# Modeling Excited States and Alignment of Energy Levels in Dye-Sensitized Solar Cells: Successes, Failures, and Challenges

Mariachiara Pastore,* Simona Fantacci, and Filippo De Angelis*

Computational Laboratory for Hybrid/Organic Photovoltaics (CLHYO), Istituto CNR di Scienze e Tecnologie Molecolari via Elce di Sotto 8, I-06123, Perugia, Italy

ABSTRACT: Theoretical and computational modeling is a powerful tool to investigate and characterize the structural, electronic, and optical properties of the main components of dye-sensitized solar cells (DSCs). In this article we focus on the description of the ground and excited state properties of both standalone and TiO_2-adsorbed metallorganic and fully organic dyes, relevant to modeling the dye→semiconductor electron injection process, which is the primary charge generation step in DSCs. By reviewing previous data from our laboratory, integrated with new calculations, we wish to critically address the potential and limitations of current DFT and TDDFT computational methods to model DSCs. While ruthenium dyes are accurately described by standard DFT approaches, for highly conjugated organic dyes, characterized by strong charge transfer excited states, specifically tailored exchange-correlation functionals are needed. For ruthenium dye/ semiconductor interfaces, a strategy is presented, which accurately describes the electronic and optical properties *and* the alignment of ground and excited state levels at the same time, allowing us to discuss the coupling and the energetics of the excited states underlying the ultrafast electron injection. For donor–acceptor organic dyes, a simple picture based on the dye lowest unoccupied molecular orbital (LUMO) broadening accounts for the different interfacial electronic coupling exhibited by dyes with different anchoring groups. The explored DFT/TDDFT methods, however, are not capable to deliver at the same time a balanced description of the dye@TiO_2 excited states and of the alignment of the dye excited states with the semiconductor manifold of unoccupied states. This represents a challenge which should be addressed by next generation DFT or post-DFT methods.
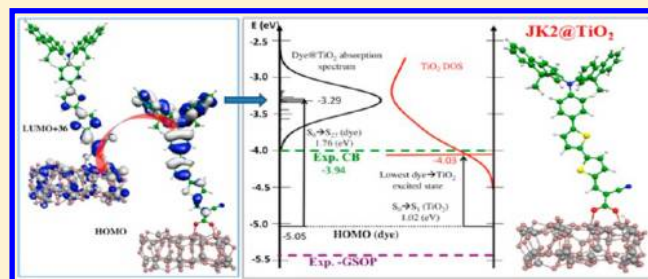
1. INTRODUCTION

Within today's global challenge to exploit solar energy for sustainable development, dye-sensitized solar cells (DSCs) represent a particularly promising alternative to traditional silicon-based solar technologies to the direct conversion of light into electrical energy at low cost and with high efficiency.[1] A schematic representation of the key components, energetics, and basic operational mechanism of DSCs is shown in Figure 1.

The heart of the device consists of a mesoporous oxide layer, usually composed of TiO_2 or ZnO nanoparticles (gray spheres in Figure 1), which is deposited onto a transparent conducting oxide (TCO in Figure 1) on a glass or plastic substrate. Grafted on the surface of the nanocrystalline oxide is a monolayer of sensitizing dye (red spots in Figure 1), which absorbs the solar radiation, 1, and injects the ensuing photoexcited electrons, 2, into the manifold of unoccupied semiconductor states, which we hereafter refer to as conduction band (CB, in Figure 1); the concomitant hole is transferred to the redox mediator (typically I^-/I_3^- or Co(II)/Co(III) in an organic solvent or a solid state hole conductor), 3, which is regenerated by a catalyst (usually metallic Pt) at the counter-electrode, 4, closing the circuit. The generated potential difference (the open circuit voltage of the cell, V_{oc}) is the difference between the quasi-Fermi level of the semiconductor under illumination (blue dashed line in Figure
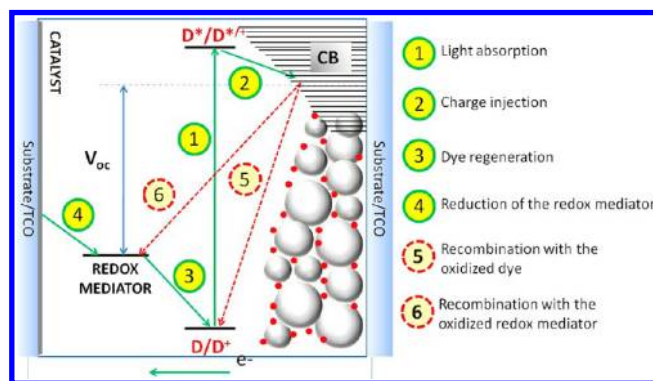

Figure 1. Schematic representation of the constituent materials and energy levels of a DSC along with forward (green lines) and backward (dotted red lines) electronic processes. The energy levels roughly correspond to those of a DSC based on the N3 dye (red spots), TiO_2 nanoparticles (gray spheres), and I^-/I_3^- redox mediator (not shown).

1) and the redox potential of the mediator. The corresponding overall efficiency of the cell is defined as

$$\eta = \frac{V_{OC}J_{SC}FF}{P_I} \qquad (1)$$

where J_{SC} is the photocurrent density at short circuit; FF is the fill factor; and P_I is the intensity of the incident light. The overall DSC performance is strongly determined by the efficiency of the various desired electron transfer and charge transport processes (1−4 in Figure 1) against the recombination losses (5 and 6 in Figure 1). In particular, the monochromatic incident photon to current conversion efficiency (IPCE) of the solar cell under short circuit conditions, whose integral over the solar spectrum gives the short circuit photocurrent J_{SC}, is defined as

$$IPCE = LHE \times \phi_{INJ} \times \phi_{COLL} \qquad (2)$$

where LHE is the light harvesting efficiency of the photoelectrode; ϕ_{INJ} is the quantum yield of electron injection; and ϕ_{COLL} is the electron collection efficiency at the TCO.

Among other factors, crucial parameters affecting the DSC efficiency are therefore the optical,[2,3] photoelectrochemical,[4,5] and structural properties of the dye sensitizer.[6−12]

In this work, we focus on the modeling of dye/TiO$_2$ excited state properties relevant to optical absorption and electron injection to the semiconductor CB states, which are the primary charge generation events occurring at the dye/semiconductor interface and which both contribute to the photocurrent generation and thus to the overall DSC efficiency according to eq 2.

Considering the charge injection as a nonadiabatic radiationless process,[13] the injection rate, eq 2, depends on two factors: (i) the squared electronic coupling matrix element between the donor and the acceptor ($|H|^2$ in eq 3) and (ii) the Franck−Condon weighted density of states (FCWD in eq 3), which is a function of the reorganization energy λ and of the driving force $\Delta G°$ (see Figure 2 and eq 4).[13] The coupling is a function of the spatial and energetic overlap between donor and acceptor states. The driving force is related to the alignment of dye/semiconductor energy levels and the density of unoccupied semiconductor states, which therefore both contribute to the effectiveness of the electron injection process. The reorganiza-

tion energy, together with the driving force, define the probability to reach an isoenergetic nuclear configuration where the donor−acceptor electronic states have the same energy. Notice that for a large number of acceptor states, which is typical of semiconductors (Figure 2), the FCDW reduces to a pure density of states (right-hand side of eq 3).[13,14]

$$k_{et} = \frac{2\pi}{\hbar}|H|^2 FCWD = \frac{2\pi}{\hbar}|H|^2\rho(E) \qquad (3)$$

$$FCWD = \frac{1}{\sqrt{4\pi\lambda k_b T}}\exp\left(-\frac{(\lambda + \Delta G)^2}{4\lambda k_b T}\right) \qquad (4)$$

On the basis of the above considerations, a potential highly efficient dye sensitizer dye should be endowed by a wide and intense optical absorption spectrum, associated to a long-lived charge-separated excited state, possibly strongly coupled to the oxide CB states as well as ground and excited state oxidation potentials which properly match the redox potential of the mediator and the semiconductor CB, respectively (Figure 1). Traditionally, the most commonly employed dyes in DSCs are ruthenium(II) polypyridyl complexes.[15−17] Recently, Zn(II)-porphyrins have reached high efficiency when coupled to Co(II)/Co(III) redox shuttles, exceeding 12%.[18] Fully organic dyes have also attracted considerable interest,[15,19] in light of their superior synthetic flexibility, scalability, and reduced environmental impact (see refs 20 and 21 for a detailed overview); in conjunction with transition metal-based electrolytes, organic dyes have been shown to clearly outperform Ru(II)-based dyes.[22−26] The most efficient organic sensitizers have typically a D−π−A structure, with the donor group (D) being an electron-rich unit, linked through a conjugated linker (π) to the electron acceptor group (A), which is directly bound to the semiconductor surface, usually through a carboxylic or cyanoacrylic function.

Theoretical modeling of isolated cell components (e.g., dye, semiconductor nanoparticles, electrolyte, etc.) as well as of combined dye/semiconductor/electrolyte systems[27,28] can successfully assist the experimental research by providing in silico design of new sensitizers and a deeper comprehension of the basic chemical physics processes governing the cell functioning and its performances. A computational approach to DSC modeling can be essentially casted into a stepwise problem, whereby one first needs to accurately simulate the individual DSC components, consisting of a minimum of the dye and a model semiconductor. The fundamental information amenable to simulation at this stage is the dye geometrical structures, ground state oxidation potential, optical absorption spectra, and excited state oxidation potential and the semiconductor CB energy and/or density of states and its band gap. For the interacting dye/semiconductor, one needs to calculate the dye adsorption modes onto the semiconductor, the nature and localization of the dye@semiconductor excited states, and the alignment of ground and excited state energy levels at the dye/semiconductor heterointerface, which, along with an estimate of the electronic coupling, constitute the fundamental parameters ruling the electron injection and dye regeneration processes.

Modern first-principles computational methodologies, such as those based on density functional theory (DFT) and its time dependent extension (TDDFT), provide the theoretical/computational framework to describe most of the desired properties of the individual dye/semiconductor systems and of
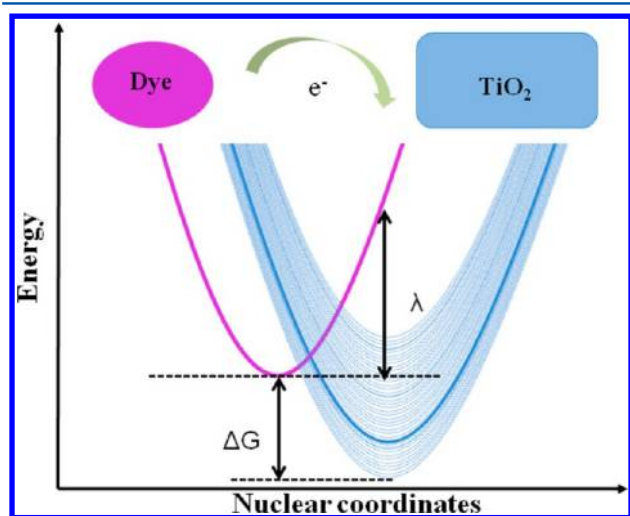

Figure 2. Energetics of the electron transfer process between a donor (left side) and a quasi-continuum of acceptor states (right side) typical of dye sensitization of a semiconductor.

their interface. The information about the dye-sensitized interface extracted from these calculations constitutes the basis for the explicit simulation of the photoinduced electron transfer by means of quantum or nonadiabatic dynamics. The dynamics introduces a further degree of complexity in the simulation, due to the simultaneous description of the coupled nuclear/electronic problem. Various combinations of electronic structure/excited states and nuclear dynamics descriptions have been applied to dye-sensitized interfaces.[29−32] In most cases, these approaches rely either on semiempirical Hamiltonians[33−35] or on the time-dependent propagation of single particle DFT orbitals,[36,37] with the nuclear dynamics being described within mixed quantum-classical[29,30,34,38] or fully quantum mechanical approaches.[37] Real-time propagation of the TDDFT excited states[39] has also emerged as a powerful tool to study photoinduced electron transfer events, with applications to dye-sensitized interfaces based on mixed quantum-classical dynamics.[32,40]

While DFT and TDDFT can in some cases accurately describe the properties of dye-sensitized interfaces, the simulation of the excited state properties of D−π−A organic dyes and of the corresponding dye-sensitized TiO$_2$ interfaces still represents an open issue, due to the problematic description by conventional exchange-correlation functionals of the charge transfer excitations typical of D−π−A organic dyes and consequently of the related dye-sensitized interfaces. By contrast, the simulation of the electronic and optical properties of Ru(II)-polypyridine dyes has been successfully accomplished with standard DFT/TDDFT methods.[16,41−43] This success has opened the way to the investigation of various fundamental aspects of dye/semiconductor interfaces such as the effect of acid/base chemistry, solvent and counterions, dye adsorption mode, and surface dipoles, providing some deeper knowledge of the functioning of this fundamental class of solar cells sensitizers.[3,5,44−47] Furthermore, several new dyes have been computationally designed and screened before their synthesis, thus allowing for a considerable saving of resources and contributing to some advances in the DSC field.[48]

In this article, we address the problem of providing a unified modeling of the electronic structure and excited states of the joint dye/semiconductor system for both metallorganic and organic dye-sensitized TiO$_2$ surfaces, with emphasis on the crucial electronic, optical, and energetic parameters affecting the light harvesting and the electron injection processes. In the first part of the manuscript, we shall deal with the description of the spectroscopic and redox properties of stand-alone sensitizers, reviewing the computational strategies leading to accurate excitation energies and ground and excited state oxidation potentials for both Ru(II) and metal-free dyes.[2,4,5,42] We show that while conventional DFT approaches[49] accurately reproduce the electronic structure of Ru(II) sensitizers the calculation of the excited states of realistic organic dyes requires the use of properly calibrated computational approaches.

Moving to the description of dye/TiO$_2$ interfaces, in the second part of the paper, we shall discuss the merits of various DFT/TDDFT approaches to the description of the electronic structure of the joint dye@TiO$_2$ system. In line with the results for standalone dyes, we show that for Ru(II)-dye-sensitized TiO$_2$ surfaces one can simultaneously obtain an accurate ground and excited state description. For highly conjugated D−π−A organic sensitizers, currently available TDDFT methods do not deliver at the same time accurate excitation energies and a correct alignment of energy levels. As a matter of

fact, the simultaneously accurate description of dye/TiO$_2$ excited states and energy level alignment for such systems remains a challenge to be addressed by next generation DFT/TDDFT or post-DFT computational methods.

2. SPECTROSCOPIC AND REDOX PROPERTIES OF DYE SENSITIZERS

The very basic requirements for a potentially efficient dye sensitizer are: (1) as wide as possible absorption range; (2) high molar extinction coefficient to maximize light harvesting; and (3) fast electron injection and dye regeneration processes. Previous experience with various dyes has shown that efficient electron transfer requires the excited state oxidation potential (D*/D*$^{/+}$ in Figure 1, hereafter ESOP) and ground state oxidation potential (D/D$^+$ in Figure 1, hereafter GSOP) to be slightly (∼0.2 eV) lower (more negative) and higher (more positive) than that of the TiO$_2$ CB and the redox mediator potential, respectively.[50] The fine-tuning of the minimum driving force to effectively accomplish electron injection and regeneration processes is intensively investigated[23,51] since reducing energy losses in both processes can lead to the simultaneous increase of both photocurrent (by virtue of the diminished dye energy gap) and open circuit voltage (by exploiting redox shuttles with higher potential compared to the TiO$_2$ CB).

Due to the large size and the complexity of the investigated systems, DFT and TDDFT are the methods of choice to simulate the structural, electronic, and spectroscopic properties of dye sensitizers matching the above requirements.[52,53] We briefly recall that DFT is a ground state technique, and it provides us with geometrical structures and single particle energy levels and orbitals (e.g., HOMO and LUMO). The core of any DFT scheme is the exchange-correlation (x-c) functional, which describes electron−electron interactions, for which various approximate forms exists. TDDFT allows us to describe excited states by delivering the system's response to the oscillating electric field in terms of a series of coupled occupied to virtual orbital excitations, which are mixed by appropriate coefficients to deliver the desired excited state. As such, DFT orbitals constitute the basis for TDDFT calculations and may provide some approximate description of the system's excited states.

For a meaningful comparison of the calculated properties with the corresponding experimental quantities,[41,54] solvation effects should also be modeled, with nonequilibrium solvation to describe excited states.[55] While explicit inclusion of solvent molecules is obviously the "exact" way of treating solvation effects,[47,56−58] it involves a huge increase in the dimensions of the system and associated computational overhead. Inclusion of solvation effects is therefore routinely introduced by means of continuum solvation models,[59] although explicit inclusion of solvent molecules in model dye/TiO$_2$ interfaces has also recently been reported.[47,56,60]

The rigorous way to obtain the system's GSOP is to evaluate the Gibbs free energy difference between the neutral and the oxidized GS species at their relaxed geometries, $(G^0 − G^+)_{GS}$, which is conveniently accessed by combining calculations in vacuo and in solution.[5] The calculated values can be compared to electrochemical measurements (e.g., cyclic voltammetry data), provided the potential of the reference electrode used for measurements is known against the vacuum level.[61] An approximate vertical GSOP estimate can be obtained within Koopman's theorem, by simply taking the negative of the
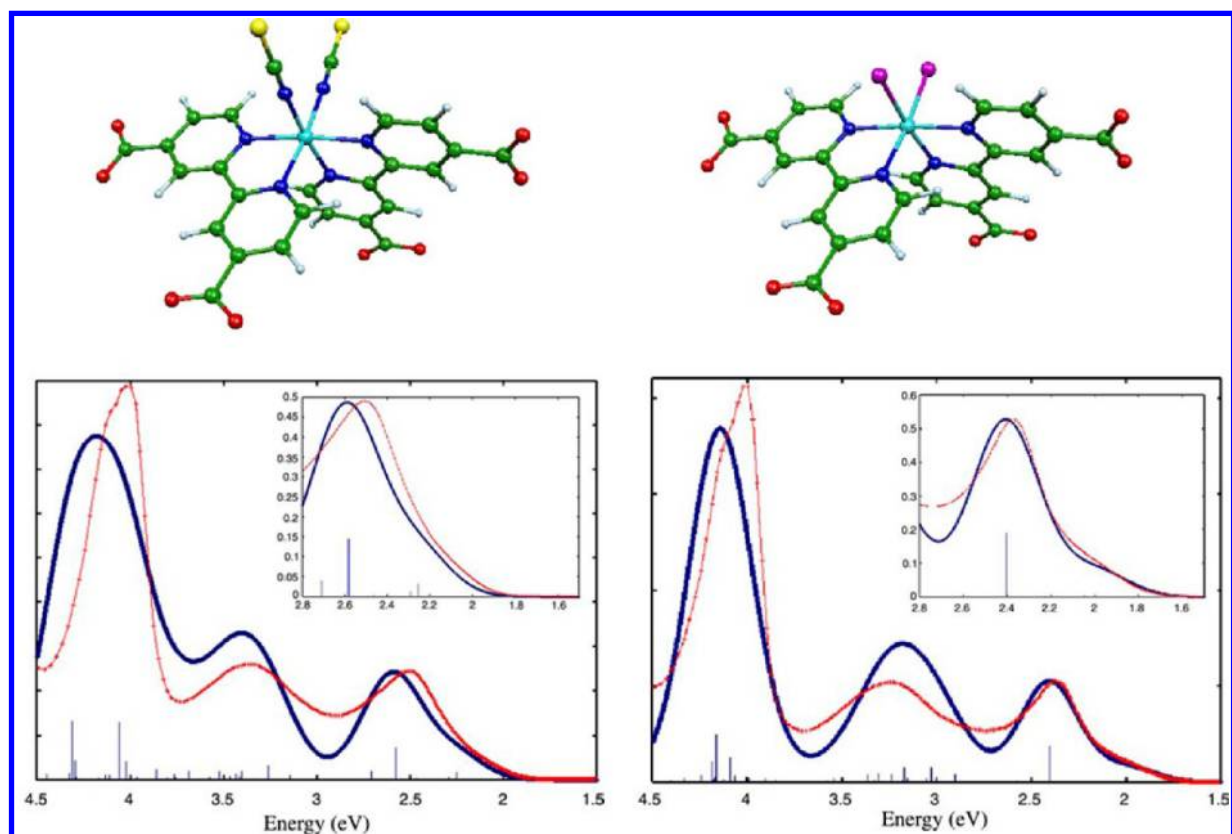
C

dx.doi.org/10.1021/jp3095227 | J. Phys. Chem. C XXXX, XXX, XXX−XXX

Figure 3. Top: Optimized molecular structures of the *cis*-[Ru(4,4′-COO-2,2′-bpy)$_2$(X)$_2$]$^{4-}$, X = NCS (left) and Cl (right), complexes. Bottom: Comparison of the calculated (blue lines) absorption spectrum of the samecomplexes, X = NCS (left) and Cl (right), with the corresponding experimental spectra (red lines) in water solution. Inset: detail of the low-energy spectral region. Energy in eV. The intensity of the experimental spectrum has been rescaled so that the intensity of the experimental and calculated absorption maxima of low-energy bands matches.

HOMO energy. The ESOP is obtained as the free energy difference between the neutral and the oxidized species in the excited state, taken at their respective equilibrium geometries. Experimentally, the ESOP is estimated by subtracting the adiabatic lowest excitation energy (E_{0-0}) from the GSOP according to eq 4[50]

$$\text{ESOP} = (G^0 - G^+)_{ES} \approx (G^0 - G^+)_{GS} - E_{0-0} \qquad (5)$$

where $(G^0 - G^+)_{ES}$ is the exact ESOP and $(G^0 - G^+)_{GS}$ is the exact GSOP. Having the GSOP, we need an estimate of the adiabatic lowest transition energy, E_{0-0}, to calculate the ESOP. A first approximation to E_{0-0} is to neglect relaxation of the excited state and to take the lowest vertical excitation energy. The rigorous calculation of E_{0-0} instead considers the energy difference between the optimized ground and excited state geometries, possibly including the change in the zero-point energy.

The optimization of the ground state geometries of the standalone Ru(II) dyes has been carried out with the Gaussian 03 code,[62] using the 3-21G* basis set and the standard B3LYP functional.[49] The singlet→singlet and singlet→triplet vertical excitation energies and oxidation potentials were calculated using the DGDZVP basis and the B3LYP method (see refs 5 and 42 for further details). For the organic sensitizers reported in the present study, the ground state geometries of both protonated and deprotonated dyes were optimized at the B3LYP/6-31G* level of calculation. We previously found that ground state geometry optimization by B3LYP leads to slightly improved excitation energies compared to geometries opti-

mized by MPW1K.[2] For the TDDFT calculations, three different x-c functionals have been used: the two hybrid B3LYP[49] and MPW1K[63] functionals and the Coulomb attenuated B3LYP (CAM-B3LYP) approach, as implemented in Gaussian 09 (G09).[64] For the calculation of ΔG_{ox} we adopted a 6-31+G* basis set, which includes both diffuse and polarization functions. We tested the performance of different GGA, hybrid GGA, and meta-hybrid GGA functionals, also combining different exchange and correlation parts, to elucidate the combined effect on the computed ΔG_{ox} of the local and nonlocal HF exchange as well as of the correlation functional. The TDDFT excited state geometry optimizations were performed with the TURBOMOLE program package,[65,66] employing the SV(P) basis set[67] and two hybrid x-c functionals with increasing amount of Hartree-fock exchange, namely, the B3LYP[68] and the BHLYP functionals,[49,69,70] the latter showing an increased percentage of HF exchange (50 vs 20%). In this case, geometry optimization of both ground and excited states was performed in the gas phase.

2.1. Ruthenium Dyes. The prototype ruthenium solar cells sensitizer is the so-called N3 dye, *cis*-[Ru(4,4′-COOH-2,2′-bpy)$_2$(NCS)$_2$], which, together with its doubly deprotonated TBA salt, N719, still constitutes a fundamental benchmark for DSCs, with efficiency exceeding 11%.[16] At pH > 11, corresponding to full deprotonation of the four acidic terminal carboxylic groups, the N3 dye exhibits main spectral features in the visible and UV region, at 2.48, 3.33, and 4.07 eV, which are responsible for the characteristic red color of the dye. The related complex in which the NCS$^-$ groups are replaced by a

Table 1. Calculated HOMO (ε) Energy, GSOP, Singlet–Triplet ($S_0 \rightarrow T_1$) and Singlet–Singlet Excitation Energies ($S_0 \rightarrow S_1$), Excited State Oxidation Potentials Obtained Using Koopman's Theorem-Based GSOP and $S_0 \rightarrow T_1/S_0 \rightarrow S_1$ ($ESOP_K^T$ and $ESOP_K^S$, Respectively), and Experimental GSOP and ESOP (vs NHE) for N3 and N719 Sensitizers[a]

	calcd data				exptl data	
dye	$-\varepsilon_{HOMO}$	GSOP	$S_0 \rightarrow T_1$ ($S_0 \rightarrow S_1$)	$ESOP_K^T/ESOP_K^S$	GSOP (vs NHE)	ESOP (vs NHE)
N3	5.72	5.50 (1.06)	1.76	3.96/3.79	1.10[50]	−0.65[50]
	(1.28)		1.93	(−0.48/−0.65)		
N719	5.49	---	1.87	3.63/3.49	0.80[71]	−0.98[16]
	(1.05)	---	2.00	(−0.81/−0.95)		

[a]Values refer to the vacuum; values in parentheses refer to the NHE potential, set 4.44 eV below the vacuum level. All energies in eV.

Cl⁻ ligand complex has attracted considerable interest due to its red-shifted visible absorption bands (2.38, 3.25, and 4.03 eV) (see Figure 3).

In the bottom panel of Figure 3, the absorption spectra of the NCS and Cl complexes calculated in water solution by B3LYP/DGDZVP are compared to the experimental spectra for the two species.[30] Within the considered energy range, the spectra of both complexes show two bands in the visible, assigned to mixed ruthenium–NCS (or Cl) to bipyridine–π^* transitions rather than to pure metal-to-ligand charge-transfer transitions, and one band in the UV, arising from intraligand bipyridine $\pi \rightarrow \pi^*$ transitions. The agreement between the calculated and experimental spectra is excellent, in terms of both band separations and relative intensities of the main spectral features. Most notably, our calculations reproduce the observed red-shift of the visible and near-UV bands in the Cl complex spectrum, as well as the appearance of a low-energy shoulder (inset of Figure 3). Also in agreement with the experiment, the calculated absorption maxima of the band in the UV are at essentially the same energy in the two complexes.[42] Notice that the spectra in Figure 3 were obtained by a convolution of singlet–singlet excitations, which due to the neglect of spin–orbit coupling in our calculations are the only transitions to determine the spectral shape. Our results suggest that the shoulder in the low-energy region is also due to singlet–singlet excitations. Preliminary TDDFT calculations including the effect of spin–orbit coupling suggest a minor impact of singlet–triplet excitations in the overall spectral profile of the N3 dye, which induces only a slight intensity increase on the red wing of the spectrum.

The GSOP and ESOP of the N3 and N719 dyes were earlier reported by us,[5] and a summary of the results is collected in Table 1. While the GSOP of the two dyes was rigorously calculated, for computational convenience we simply approximated E_{0-0} with the lowest vertical excitation energy of the system at the ground state geometry, considering both singlet–singlet and singlet–triplet excitation energies. With this approximation, however, the calculated ESOP values could be overestimated.

The calculated GSOP for the N3 dye is in excellent agreement with the 1.10 V oxidation potential reported in ref 50. The Koopmans' theorem estimate of the GSOP is, as expected, higher than its adiabatic counterpart, due to the neglect of relaxation effects of the oxidized dye. For the N719 dye the HOMO is destabilized compared to N3, due to the increased overall charge donation to the metal. The 0.23 eV energy upshift is in excellent agreement with the 0.30 V decrease in oxidation potential measured experimentally.[71]

Experimentally, ESOP estimates of −0.65 and −0.98 V versus NHE have been reported for N3 and N719, respectively.[16,50]Remarkably, the absolute ESOP values are in

good agreement with the experiment, with values obtained using $S_0 \rightarrow S_1$ transitions (−0.65 and −0.96 eV) reproducing almost exactly the experimental values.

In summary, our results show that the "standard" B3LYP method together with solvation effects is capable of accurately reproducing the electronic and optical properties of the most commonly employed ruthenium dye sensitizers.

2.2. Organic Dyes. A different situation is found for push–pull organic sensitizers for which the accurate calculation of excitation energies still represents Achille's heel of standard TDDFT approaches, although some successful strategies have been proposed in various benchmark and calibration studies.[2,4,72,73] Conventional DFT x-c functionals yield large underestimations for excited states with a significant long-range CT character and in the case of molecules with spatially extended π systems.[73–75] For Ru(II) complexes, the CT problem is limited to some extent by the substantial overlap of metal and ligand states characterizing the starting and arriving orbitals in metal-to-ligand charge transfer (MLCT) excitations typical of Ru–polypyridine complexes. The use of tailored hybrid functionals, incorporating a variable amount of nonlocal Hartree–Fock (HF) exchange, partially corrects the wrong asymptotic behavior. This is however a practical strategy rather than a reliable solution since the extent of the HF exchange remains strongly system dependent.[54,73,76] Alternative methodological approaches use an increasing fraction of HF exchange as the interelectronic separation increases; the long-range corrected (LC) functionals[77–80] and the Coulomb-attenuating B3LYP (CAM-B3LYP) method[81] belong to this family of range-separated functionals.

Here we shall discuss the TDDFT results for two representative dye sensitizers, selected among the highest-efficient ones and having different electron donor and acceptor groups: the JK2[82] dye has a TPA-like donor (N,N-bis(9,9-dimethylfluorene-2-yl)phenyl), with a cyanoacrylic acid as an anchoring unit, while the D102 dye[83,84] has indoline and rhodanine-3-acetic acid as electron donor and acceptor groups, respectively (see Figure 4).

In Table 2 we report the calculated lowest excitation energies for the protonated (1H) and deprotonated (0H) JK2 and D102 in the gas phase and ethanol solution along with the corresponding experimental absorption maxima. We notice that, going from the gas phase to ethanol solution, a decrease of the lowest excitation energy is observed; such a red-shift, regardless of the x-c functional employed, is in the range 0.15–0.35 eV and arises from the stabilization of the charge-separated excited state by the solvent. On the other hand, deprotonation of the carboxylic moiety may lead to a substantial blue-shift of the lowest excitation energy. Deprotonation of the conjugated cyanoacrylic acid in JK2 gives rise to a large blue-shift, by ca. 0.3–0.4 eV, compared to that predicted for the nonconjugated
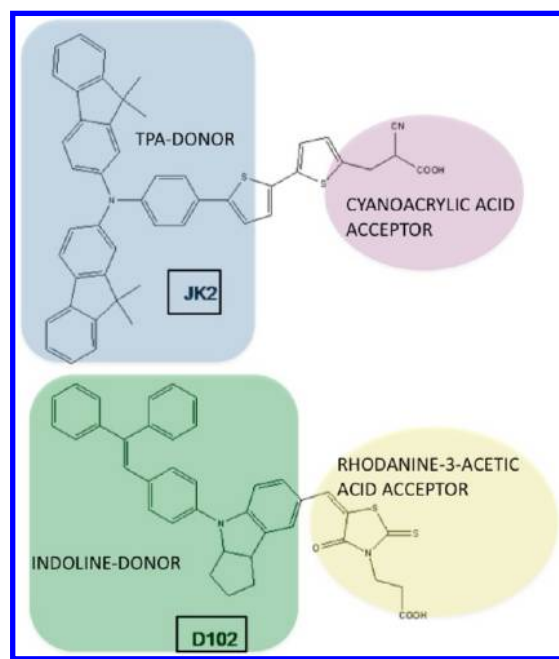
E

dx.doi.org/10.1021/jp3095227 | J. Phys. Chem. C XXXX, XXX, XXX–XXX

Figure 4. Molecular structures of the JK2 and D102 dye sensitizers.

rhodanine-3-acetic acid in D102, which is ca. 0.1 eV. For JK2 we expect spectral data in ethanol to be somehow intermediate between those calculated for protonated and deprotonated species. With reference to solution data, we calculate 2.45–2.81 (MPW1K) and 2.79–2.94 (CAM-B3LYP) excitation energies for protonated/deprotonated species (1H or 0H in Table 3), in good agreement with the experimental absorption maximum of 2.84 eV. The MPW1K functional slightly underestimates the electronic transitions for JK2, possibly due to the static description of Hartree–Fock exchange with the interelectronic distance, which introduces a rigid system-independent shift of the transition energies.[85,86]

Looking at the calculated data for the D102 sensitizer, we find a somehow similar trend, although in this case both MPW1K and CAM-B3LYP seem to overshoot the experimental absorption maximum of 2.53 eV, with 1H/0H values of 2.78–2.89 and 2.86–2.90 eV, respectively. The B3LYP functional, on the other hand, delivers a lowest excitation of 2.29–2.37 eV for 1H/0H cases, thus underestimating the experimental absorption maximum energy. Clearly the two dyes have quite a different response to the choice of the x-c functional. This system-dependent variability imposes a careful a priori calibration of the computational protocol, including solvent effects and a careful analysis of the anchoring group acid–base chemistry.

Here we discuss the calculation of the GSOP and ESOP for a set of four TPA-based dyes,[19] which only differ by the increasing degree of conjugation from L0 to L4 (see Figure

5).[4] Although B3LYP usually provides quite accurate ground state geometries, even for large push–pull molecules, it is clear that the underestimation of the energy of CT states may represent a serious issue upon excited state geometry optimization, required to calculate the adiabatic transition energy. The erratic lowering of the excitation energy, as the CT character increases, could lead to artificial minima on the excited state energy surface.[4,85,87−89] Again, the use of either hybrid functionals with a large fraction of Hartree–Fock exchange (ca. 50%) or long-range corrected approaches provides a valuable way to overcome the problem of obtaining artificially distorted excited state equilibrium geometries.[4]

Calculated GSOPs are reported in Table 3. As it can be noticed, the MPW1K functional[63] is the method that provides results closer to the experimental values, with the largest deviation amounting to 0.28 eV for L4. We also notice that the accuracy of the MPW1K results, as for all the methods employed here, slightly decreases as the dimensions and conjugation of the molecules increase, as signaled by the overestimate of the difference between the GSOP for L0 and L4 (Table 3). The error, however, is not dramatic considering the size of the systems and the number of combined calculations required to obtain the GSOP. Interestingly, increasing the fraction of Hartree–Fock exchange does not improve the accuracy of the calculated GSOPs along the series.

Contrary to what was found for Ru(II)-based dyes, Table 3 shows that Koopman's theorem delivers large overestimation/underestimation compared to the experimental GSOPs by varying the functional. In particular, one can notice that for the pure GGA functionals the underestimation is more severe for the larger L3 and L4 dyes, exceeding 1 eV in the case of MPWLYP. On the other hand, for all the hybrid approaches, the estimated oxidation potentials turn out to be too high, as a consequence of the down-shift of the energy levels of the occupied MOs induced by the nonlocal Hartree–Fock exchange;[48] in this case, the deviation from the experimental results decreases as the size of the molecules increases. Therefore, for dyes with moderate conjugation, B3LYP provides HOMO levels which reproduce the GSOP, and while increasing the molecular size and the length of the electron conjugation (delocalization), the use of a larger fraction of nonlocal Hartree–Fock exchange is required to get reliable estimates.

A comparison of calculated and experimental adiabatic excitation energies for the same dyes set in acetonitrile solution is reported in Table 4. As it can be noticed, an overall good agreement between calculated and experimental data is found, although a slight underestimation of experimental quantities is observed by increasing the dye molecular size.

To provide a unified representation in terms of calculated versus experimental GSOP and ESOP, we report in Figure 5 a survey of both data sets, along with the energetic positions of the TiO$_2$ conduction band and I^-/I_3^- redox potentials.

Table 2. Computed and Experimental Excitation Energies (in eV) of the Lowest Excited State of JK2 and D102 in the Gas Phase and EtOH Solution

	B3LYP			MPW1K			CAM-B3LYP			
	1H		0H	1H		0H	1H		0H	
dye	vac	solv	solv	vac	solv	solv	vac	solv	solv	exp. (EtOH)
JK2	1.99	1.82	2.26	2.60	2.45	2.81	2.78	2.62	2.94	2.84[82]
D102	2.61	2.29	2.37	3.07	2.78	2.89	3.11	2.86	2.90	2.53[83]

Table 3. Experimental and Theoretical GSOP (eV) in Acetonitrile of the L0, L2, L3, and L4 Dye Sensitizers[a]

	exp.[19]	MPW1K	B3LYP	BH&H	BH&H-LYP	MPW1K-LYP	MPWLYP	MPWPW91
dye	% HF	42.8	20.0	50.0	50.0	42.8	0.0	0.0
L0	5.81	5.82 (6.58)	5.66 (5.73)	5.53 (6.60)	5.56 (6.62)	5.55 (6.38)	5.33 (4.95)	5.49 (5.13)
L2	5.57	5.35 (6.09)	5.21 (5.31)	5.19 (6.10)	5.18 (6.11)	5.16 (5.89)	4.91 (4.56)	5.11 (4.76)
L3	5.51	5.33 (6.00)	5.08 (5.21)	5.09 (5.99)	5.13 (6.00)	5.08 (5.79)	4.78 (4.48)	4.96 (4.68)
L4	5.45	5.17 (5.86)	4.99 (5.09)	4.98 (5.84)	5.00 (5.86)	5.00 (5.64)	4.70 (4.41)	4.86 (4.57)
ΔL0/L4	0.36	0.65 (0.72)	0.67 (0.62)	0.55 (0.76)	0.56 (0.76)	0.55 (0.74)	0.63 (0.54)	0.63 (0.56)

[a]Within parentheses, we also report the corresponding values for $-\varepsilon_{HOMO}$ (eV), calculated in acetonitrile for the neutral species at its equilibrium geometry in acetonitrile.

Table 4. Comparison between Experimental and Calculated (MPW1K/BH&HLYP/SVP) Adiabatic Lowest Excitation Energies (eV)

dye	ΔE_{0-0} (exptl)	ΔE_{0-0} (calcd)
L0	2.90	2.96
L2	2.48	2.37
L3	2.38	2.25
L4	2.35	2.14

Calculated ESOP values are in excellent agreement with experimental data (within less than 0.1 eV) for the entire series of dyes, but this agreement turns out to be partly due to the cancellation of errors occurring between the GSOP, which for the larger dyes is too negative in the NHE scale by up to 0.3 eV, and the E_{0-0} values which are underestimated by a comparable amount when increasing the dye conjugation. It is surprising to notice that the uncertainty on the GSOP is somewhat larger or comparable to that on the E_{0-0} excitation energies, the former being the difference between ground state quantities, so a better reproduction of the experimental values might be expected. Moreover, while the slight deterioration of E_{0-0} values with increasing CT is expected and can be solved by the use of range-separated functionals, the small albeit sizable inaccuracy on GSOP values was traced back here to the

correlation part of the functional, which is probably more difficult to correct.

To summarize this section, our results show that a properly calibrated DFT/TDDFT computational approach is capable of providing a unified description of both the absorption spectra and GSOP/ESOP values of dyes of relevant interest for the DSC technology, with an accuracy of the order of 0.2–0.3 eV, typical of current DFT-based methods.

3. ELECTRONIC STRUCTURE AND OPTICAL PROPERTIES OF DYES ON TIO₂

The complex interatomic interactions underlying dye inter-actions with the TiO₂ films employed in DSCs call for the use of accurate computational techniques, while the large dimensions of the systems to be studied substantially limit the range of useful theoretical and computational tools. The situation is even more complicated if one wishes to provide a description of properties related to excited states. An overview of the computational approaches and strategies to study dye/TiO₂ interfaces can be found in ref 90. Here we focus on the problem of defining a proper computational approach to reproduce the ground and excited state properties of the coupled dye@TiO₂ system in the case of the N719 Ru(II) dye and the two organic sensitizers, JK2 and D102. After a short section devoted to discuss the adsorption geometries, we shall present the results of TDDFT excited state calculations in
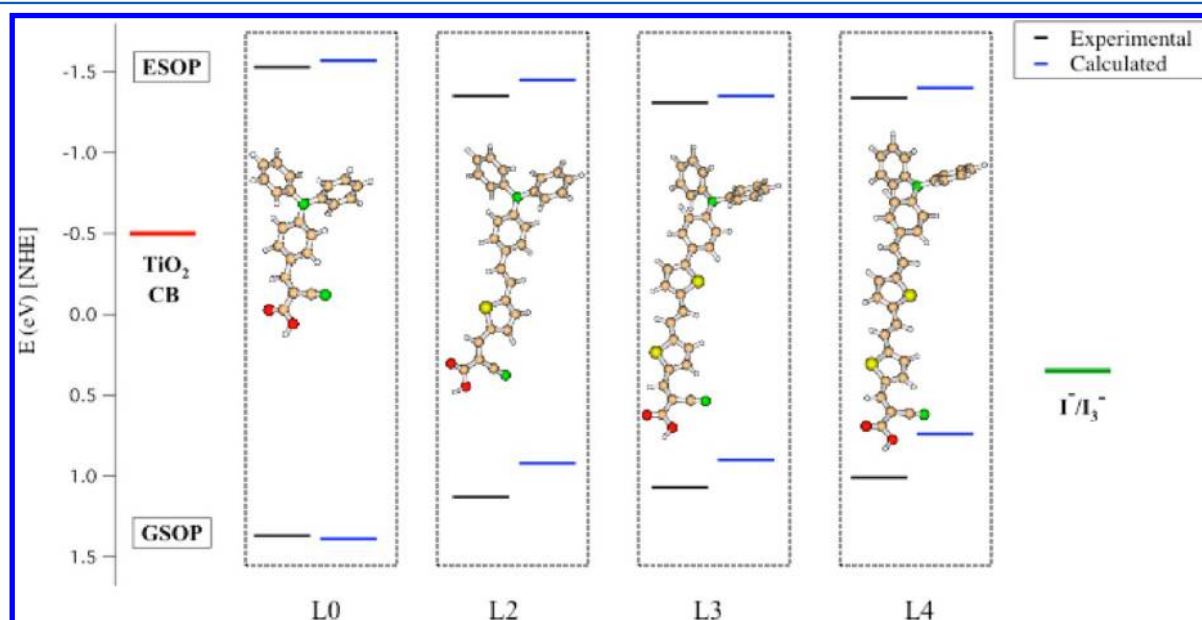

Figure 5. Schematic representation of the calculated (blue) and experimental (black) GSOP and ESOP values for the L0–L4 dye series. Energy scale (eV) referred to NHE.

solution, discussing the accuracy of different DFT x-c functionals in reproducing at the same time the absorption spectra and the energy level alignment between the dye and the TiO_2 conduction band. The implications of the picture extracted from our calculations for electron injection are also presented.

3.1. Adsorption Geometry. The first crucial step for the computational description of the dye@TiO_2 interface is the determination of the dye anchoring geometry, as the bonding type and the extent of electronic coupling between the dye excited state and the semiconductor unoccupied states can directly influence the cell performances.[1] Recently, it has been shown[8,91] that different anchoring groups, cyanoacrylic acid vs rhodanine-3-acetic acid, yielding different adsorption configurations and dye/TiO_2 coupling, induce different electron injection and recombination dynamics.

The anchoring mechanism of the largely employed carboxylic acid group to the TiO_2 surface can be exemplified referring to the coordination modes of the carboxylate fragment (COO^-) to metal ions; there are basically three typical coordination schemes: monodentate, bidentate chelating, and bidentate bridging.[92,93] A number of theoretical studies on the dye adsorption modes on the TiO_2 surface have been published.[3,10,28,44,45,60,91,94–104] The calculations show that for the organic dyes bearing a carboxylic acid as the anchoring group the preferred adsorption mode is bidentate bridging, with one proton transferred to a nearby surface oxygen,[10,97,105,106] while the monodentate anchoring is usually predicted to be less stable, although some dependency of the relative stability of these two anchoring modes on the employed computational methodology can be outlined.[104,107]

The geometry of N719 on TiO_2, optimized by the Car–Parrinello (CP) method,[108,109] using the PBE functional,[110] is reported in Figure 6. A stoichiometric anatase $(TiO_2)_{82}$
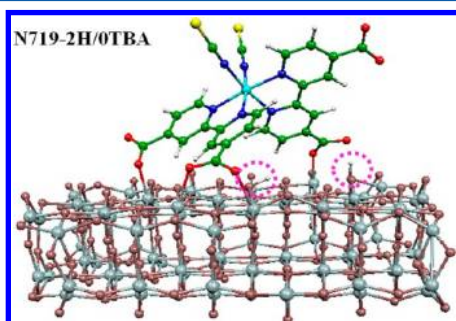

Figure 6. Optimized geometrical structure of the N719 dye with two protons and no counterions (N719–2H/0TBA) adsorbed on the $(TiO_2)_{82}$ extended model. The dotted circles denote the position of the two protons.

cluster[103,111] of nanometric dimensions exposing (101) surfaces was employed to represent the semiconductor surface. Of the three carboxylic groups involved in dye binding to TiO_2, one is attached to two surface Ti atoms in a bidentate bridging mode, while the other two are bound in a monodentate mode.[46] A report by Schiffmann et al. has confirmed that this adsorption mode is the more stable when protons are present in the combined dye/semiconductor system,[60] and recent X-ray reflectometry data lend support to this anchoring mode.[112]

Both JK2 (cyanoacrylic acid anchoring) and D102 (rhodanine-3-acetic anchoring) were found to bind to the (101) anatase TiO_2 surface in a bidentate fashion,[82] with

proton transfer to a surface oxygen. The ground state equilibrium geometries of both dyes adsorbed onto a $(TiO_2)_{38}$ cluster, displayed in Figure 7 and used for the
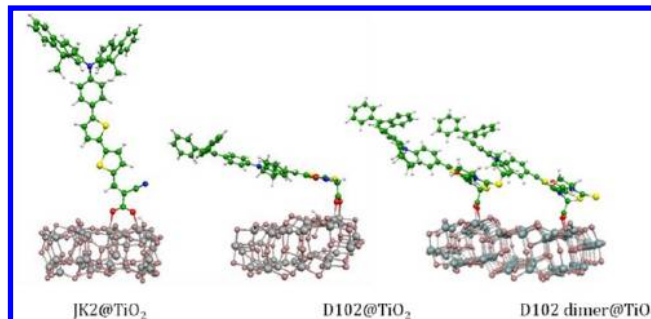

Figure 7. Optimized geometries of JK2@$(TiO_2)_{38}$, D102@$(TiO_2)_{38}$, and a D102 dimer@$(TiO_2)_{82}$.

subsequent TDDFT calculations, have been optimized in the gas phase with the ADF program package[113] employing the Becke–Perdew exchange-correlation functional[69,114] with a TZP/DZP basis set for Ti/H, C, N, O, and S. Notably, having access to the dye adsorption geometry allows us to study dye aggregates (see Figure 7 for the most stable D102 dimer on the $(TiO_2)_{82}$ cluster) and the corresponding electronic and optical properties.[10,87]

3.2. Absorption Spectra and Alignment of Energy Levels. A comparison between the experimental and calculated optical absorption spectra for N719 bound to TiO_2 is reported in Figure 8. The TDDFT calculations were performed on the GGA-optimized geometries, employing the hybrid B3LYP functional with a 3-21G* basis set. The effect of the surrounding water solvent is included by employing a polarizable continuum model of solvation (C-PCM), as implemented in the Gaussian03 program package.[62] To calculate the absorption spectrum up to ca. 2.5 eV, corresponding to the entire first visible absorption band, a large number of singlet excited states were computed (the 50 lowest transitions) with an associated large computational overhead. We also calculated the lowest 25 triplet excited states (inset of Figure 8).

The agreement between the calculated and experimental spectra in Figure 8 is excellent over the investigated energy range. The calculated spectral profile shows a shape comparable to the experimental one, with the absorption maximum being calculated at 552 nm (2.25 eV), to be compared to an experimental band maximum of 531 nm (2.34 eV). The small discrepancy between theory and experiment (<0.1 eV) seems to confirm the accuracy of the employed model and adsorption geometry. Since the use of cluster models for TiO_2 could lead to some cluster size dependency of the results,[115] we compared the present data, obtained by N719 adsorbed onto a $(TiO_2)_{82}$ cluster, with our previous data for the same dye adsorbed on the smaller $(TiO_2)_{38}$ cluster.[44] For N719@$(TiO_2)_{38}$ the TDDFT absorption maximum was calculated at 2.07 and 2.27 eV, depending on the position of the dye protons, suggesting a moderate role of the TiO_2 cluster size in determining the optical absorption of the joint dye/semiconductor system.

For N719@$(TiO_2)_{82}$, the lowest 17 TDDFT transitions, spanning an energy range between 1.58 ($S_0 \rightarrow S_1$) and 1.88 ($S_0 \rightarrow S_{17}$) eV, correspond to direct excitations from the dye HOMOs to the lowest unoccupied states of TiO_2, with
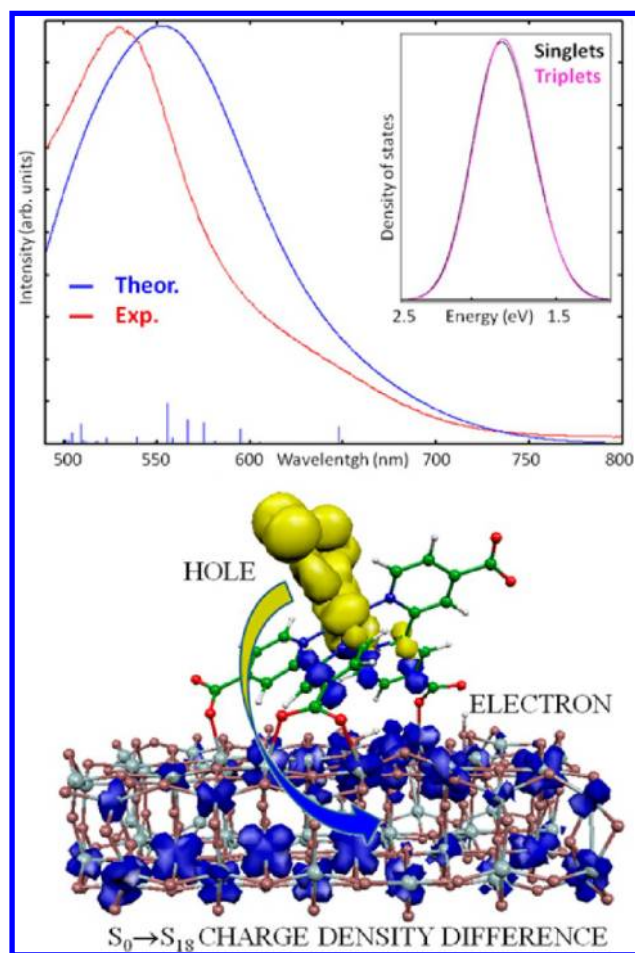
H

dx.doi.org/10.1021/jp3095227 | J. Phys. Chem. C XXXX, XXX, XXX–XXX

Figure 8. Top: Comparison between the experimental (red) and calculated (blue) absorption spectra of N719 on TiO_2. The intensity of the experimental spectrum has been rescaled so that the absorption maxima match. The inset shows the calculated density of singlet (black) and triplet (magenta) excited states (energy in eV) for the same system. Bottom: Charge density difference between the ground state (S_0) and the S_{18} excited state. A blue (yellow) color signifies an increase (decrease) of charge density upon electron excitation.

negligible oscillator strength (<0.001), i.e., a vanishingly small probability of being populated in absorption. The lowest excitation with a sizable oscillator strength is the 18th ($S_0 \rightarrow S_{18}$) excited state, which is calculated at 649 nm (1.91 eV). This transition is clearly responsible for the shoulder exhibited by the experimental absorption spectrum in exactly the same energy range (see Figure 8). Also shown in Figure 8 is the charge density difference between the S_0 ground state and the S_{18} excited state. Considering the strong admixture of dye/ semiconductor unoccupied states, the ultrafast electron injection times measured for the N3/N719 dyes on TiO_2 are not surprising.[116,117] Following visible light absorption, the excited electron is already partly delocalized into the semiconductor and only weakly interacting through the dye π^* orbitals with the charge hole localized on the Ru-NCS moieties (Figure 8). This seems an almost "direct" injection mechanism,[118] partly mediated by the dye contribution to the excited states which provides a sizable transition probability, but without the appearance of a new or shifted absorption band in the combined systems' spectrum.

We now turn our attention to the alignment of the energy levels in the combined N719@TiO_2 system. In the following,

we report the single particle energies (HOMO/LUMO) together with the TDDFT many-particle energies of the entire system, which can be directly compared on the same diagram under the assumption that the HOMO and LUMO energies are a reasonable estimate of the corresponding oxidation/reduction potentials. For such a purpose, we thus fix the relative energy scale of our system by taking as a reference the energy of the dye HOMO, which, for the isolated dye, represents a good approximation to the dye GSOP (cf. Table 1). In the combined N719@TiO_2 case, the dye-based HOMO is calculated at −5.34 eV, essentially coinciding with that of the tetraprotonated N3 dye in solution (−5.39 eV). With the estimate of dye GSOP, we can thus locate the position of the lowest TiO_2-based excited state level simply by adding the energy of the TDDFT $S_0 \rightarrow S_1$ transition (1.58 eV) to the HOMO energy (−5.34 eV), obtaining −3.76 eV for the lowest excited state localized on the TiO_2. The lowest dye-based excited state is accordingly calculated at −3.43 eV, with a corresponding lowest driving force for electron injection of ca. 0.3 eV. Considering a Nernstian behavior for TiO_2, at pH = 7 a TiO_2 flatband energy of −0.82 V vs SCE (−0.58 vs NHE) can be estimated.[119,120] Converting the energy of the NHE reference electrode in water to the vacuum scale, we can position the TiO_2 manifold of unoccupied levels at −3.86 eV vs vacuum, which is almost coincident with our estimate, although due to the limitations of our model, a comparison should be performed with some caution. Having located the dye-sensitized TiO_2 absorption onset on an absolute energy scale, we can further superimpose the density of unoccupied states in the dye-sensitized and unsensitized TiO_2 to the obtained excited state energy diagram, to provide a picture of the alignment of the absorption spectrum (mainly due to the dye transitions) and the density of TiO_2 unoccupied states. Such information is reported in Figure 9, where the energy of the lowest unoccupied TiO_2 molecular orbital of the combined system, originating the density of states (DOS) on the right side of Figure 9, has been aligned to the
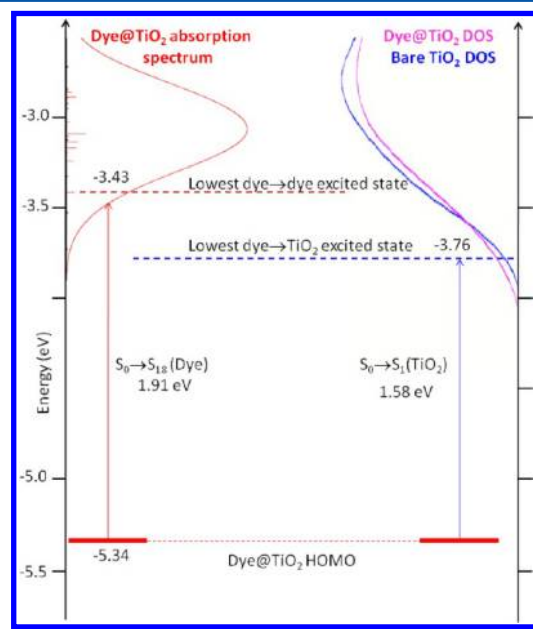

Figure 9. Left: Alignment of the ground and excited state energy levels for the interacting N719@TiO_2 system. Right: The calculated density of unoccupied TiO_2 states has been aligned to the energy of the lowest TiO_2 state in the combined system.

lowest transition of the combined N719@TiO$_2$ system. As it can be noticed, the absorption spectrum of the combined system very well matches with the density of unoccupied states in both sensitized and unsensitized TiO$_2$, with all the most intense transitions of the absorption spectrum taking place in a region of high TiO$_2$ density of unoccupied states. This is an essential requisite, along with the spatial excited state coupling, ensured by the nature of the excited states, to have the very efficient ultrafast electron injection observed in this system.

Moving to organic dyes, we report in Table 5 a survey of theoretical and experimental absorption maxima for JK2 and

Table 5. Experimental and Theoretical (DGDVPZ/Water) Absorption Maxima (in eV) for the JK2 and D102 Sensitized TiO$_2$[a]

| system | lowest dye→dye excited state | | | E_{abs} on TiO$_2$ |
	B3LYP	MPW1K	CAM-B3LYP	
JK2@(TiO$_2$)$_{38}$	1.76	2.36	2.52	2.70[97]
JK2	1.82	2.44	2.58	2.84[82]
D102@(TiO$_2$)$_{38}$	2.16	2.68	2.76	2.30[84]
D102	2.20	2.71	2.78	2.53[83]

[a]The calculated S$_0$→S$_1$ excitation for the bare JK2 and D102 at the same geometry and level of calculation is also reported.

D102 adsorbed on TiO$_2$. For the sake of comparison, we also report the corresponding excitations calculated for the protonated standalone sensitizers at the geometry optimized on the TiO$_2$ cluster at the same level of calculation. The TDDFT calculations have been performed on the GGA-optimized geometries by using the B3LYP,[49] MPW1K,[63] and CAM-B3LYP[81] functionals, the DGDZVP basis set, and taking into account the solvation effects by means of the C-PCM method implemented in G09,[64] with the default parameters of the G03 implementation.[62]

Regardless of the employed method, the results in Table 5 show that, going from the standalone dyes to the combined dye@(TiO$_2$)$_{38}$ system, a slight lowering (within 0.1 eV) in the lowest dye's excited state is predicted, which can be basically ascribed to the partial delocalization of the dye LUMO through the TiO$_2$ cluster and hence to the consequent increase of the charge transfer character of the excitation. TDDFT calculations on the dyes bound to the TiO$_2$ slab fully confirm the results obtained for the isolated dyes in solution: as we have discussed in section 2.2, CAM-B3LYP provides the best description for the JK2 sensitizer, whereas B3LYP works quite good for D102. We calculate a maximum absorption peak for JK2@TiO$_2$ at 2.52 eV, only slightly red-shifted with respect to the experimental maximum of 2.70 eV;[97] a similar red-shift is also obtained for the D102@TiO$_2$ system, where B3LYP gives a value of 2.16 eV to be compared with the experimental value of 2.30 eV.[84] The agreement between the calculated spectra and the experimental absorption maxima is remarkable and of comparable accuracy to that obtained for the dyes in solution.

So, if on the one hand we are able to predict the absorption spectra of the combined organic dye@TiO$_2$ systems, on the other hand a question arises: are we able to get a comparably accurate alignment of energy levels and extent of electronic coupling?

In Figure 10 selected isodensity plots of the dye's HOMOs and LUMOs, relevant to the discussion of the excited states for both D102@TiO$_2$ and JK2@TiO$_2$, are displayed, while in Figures 11 and 12 the corresponding dye and TiO$_2$ HOMO
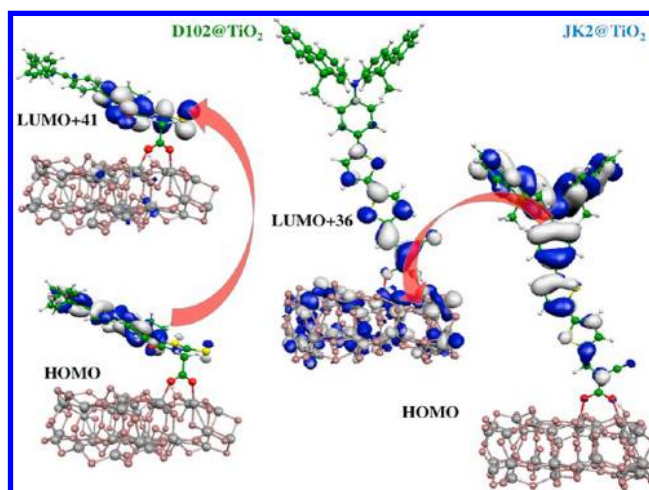

Figure 10. Isodensity plots (B3LYP/DGDZVP/water) of the dye's HOMO and LUMOs of the D102@TiO$_2$ (left side) and JK2@TiO$_2$ (right side) system.

and LUMO energy levels are schematically reported. In line with our previous work,[91] the different anchoring groups give rise to sizably different extents of state admixture between the dye and the TiO$_2$ slab (see the different profiles of the projected density of states, PDOS, reported in Figures 11 and 12). For the nonconjugated D102@TiO$_2$ system (Figure 11), a molecular orbital essentially corresponding to the pure LUMO of the dye (83% of electron density localized on the dye molecule) is calculated at −2.79 eV (B3LYP). Employing the MPW1K x-c functional yields a sizable upshift of the virtual orbitals even if it does not dramatically change the dye−TiO$_2$ state admixture, with two orbitals accounting for the dye's LUMO, located at −2.28 (ca. 13%) and −2.29 eV (ca. 70%). Also, CAM-B3LYP provides a similar picture, with even less negative unoccupied orbitals: LUMO+27 (ca. 8% of dye's electron density) at −1.76 eV and LUMO+28 at −1.75 eV (70% of dye's electron density).

Conversely, as shown by the large broadening in the PDOS in Figure 12, for the conjugated JK2@TiO$_2$ system, a strong mixing between the dye excited state and the TiO$_2$ CB states was found at all levels of calculation, with the LUMO of the dye broadened over a large number of unoccupied semiconductor states, reflecting the stronger coupling[84] characterizing dyes with a conjugated cyanoacrylic anchoring group. As shown in Figure 11, B3LYP yields the LUMO+36, having the largest dye contribution (only 13%) at −2.97 eV. The MPW1K and CAM-B3LYP functionals deliver a similar, only slightly weaker, dye/TiO$_2$ coupling and substantially up-shifted virtual orbitals, with the former predicting the LUMO+17 (ca. 20% of dye's contribution) at −2.57 eV and the latter giving the LUMO+21 (ca. 35% of dye) at −2.01 eV.

If the extent of dye−TiO$_2$ electronic coupling seems not to be extremely sensitive to the choice of the x-c functional, the alignment between the dye→dye excited state and the manifold of the TiO$_2$ CB states, as shown in Figures 13 and 14, dramatically changes by varying the nature of the x-c functional. For both D102 and JK2 cases, a substantial destabilization of the TiO$_2$ CB states is observed from B3LYP to MPW1K and CAM-B3LYP: while B3LYP delivers a reasonable value of the CB edge, −4.03 eV, a CB upshift exceeding 0.5 eV is obtained, employing the MPW1K and CAM-B3LYP functionals. More importantly, this shift toward less negative values of the

J

dx.doi.org/10.1021/jp3095227 | J. Phys. Chem. C XXXX, XXX, XXX−XXX
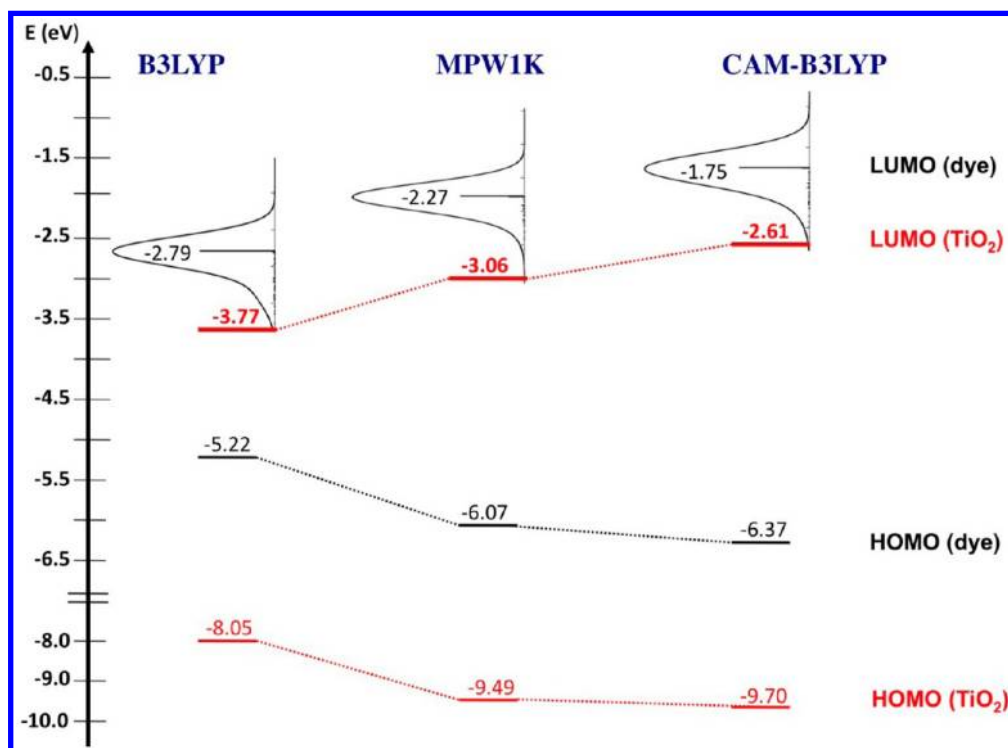
Figure 11. Scheme of the energy levels of the D102@TiO$_2$ system calculated by the B3LYP, MPW1K, and CAM-B3LYP functionals in water solution. The dye's LUMO is represented through the dye's projected density of states (PDOS).
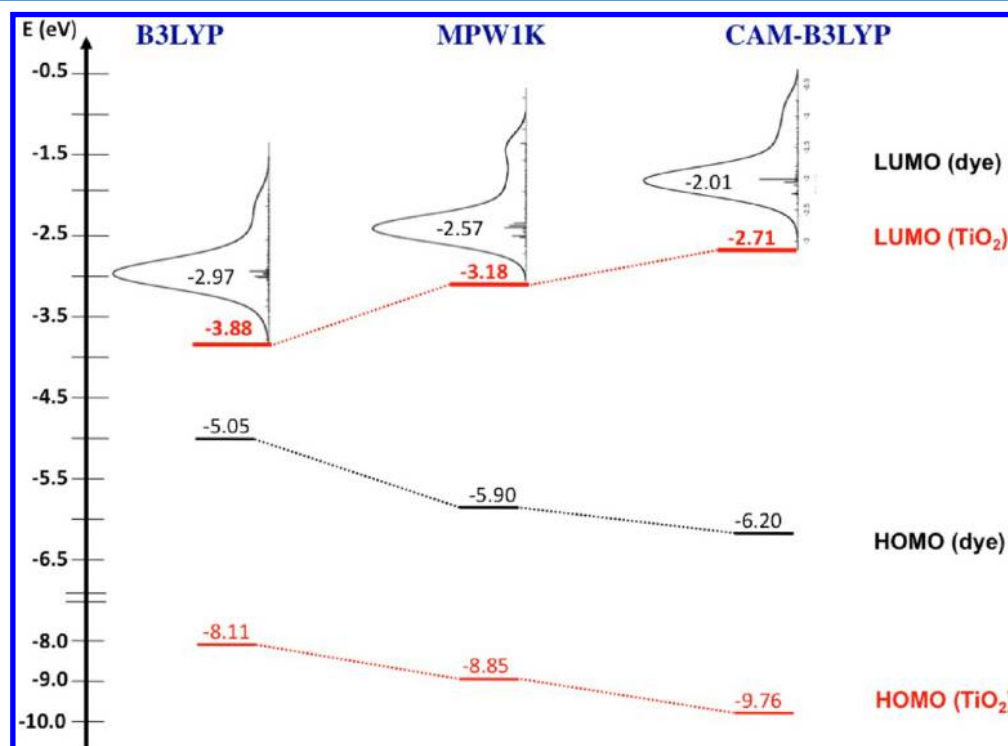
Figure 12. Scheme of the energy levels of the JK2@TiO$_2$ system calculated by the B3LYP, MPW1K, and CAM-B3LYP x-c functionals in water solution. The dye's LUMO is represented through the dye's projected density of states (PDOS).

unoccupied orbitals is not accompanied by a parallel and balanced change in the energy of the dye excited state. As a matter of fact, while B3LYP positions the absorption maximum of the dye@TiO$_2$ ca. 1.0 and 0.7 eV above the TiO$_2$ CB edge for D102 and JK2, respectively, CAM-B3LYP predicts a reversed alignment of excited state energies, with the dye@

TiO$_2$ excited state lying below the TiO$_2$ CB edge by ca. 0.1 and 0.4 eV for D102 and JK2, respectively (Figures 13 and 14).

Obviously, a totally different energetics of electron injection is predicted by the B3LYP and CAM-B3LYP functionals, with MPW1K providing an intermediate description, whereby CAM-B3LYP predicts an energetically unfavorable electron transfer

Figure 13. Alignment of the ground and excited state energy levels for the interacting D102@TiO$_2$ system together with the calculated density of unoccupied TiO$_2$ states also aligned to the energy of the lowest TiO$_2$ state in the combined system. Green and purple dotted lines indicate the experimental TiO$_2$ CB edge and dye's GSOP, respectively. Notice that we have taken minus the value of GSOP to compare it to the dye's HOMO level.

from the dye@TiO$_2$ excited state to the semiconductor manifold of unoccupied states. The situation turns out to be quite dramatic for the JK2 dye, for which the method (CAM-B3LYP) delivering the exact excitation energy for both the dye in solution and TiO$_2$-adsorbed delivers a totally unphysical alignment of energy levels. For the same dye, B3LYP offers a reasonable alignment of the dye LUMO with the TiO$_2$ CB edge but considerably underestimates the dye@TiO$_2$ absorption maximum energy. For the D102 case, on the other hand, B3LYP seems to provide a reasonably good overall alignment of energy levels, including excited states.

These results are the consequence of a different and unbalanced description of the dye and semiconductor excited (or unoccupied) states, whereby the highly conjugated JK2 dye requires a substantial amount of dynamic correlation to correct the inadequacy of the Kohn–Sham orbitals and deliver the correct excited state energy, while for TiO$_2$ the Kohn–Sham orbitals already represent an adequate description of the system's excited states.

4. CONCLUSIONS AND PERSPECTIVES

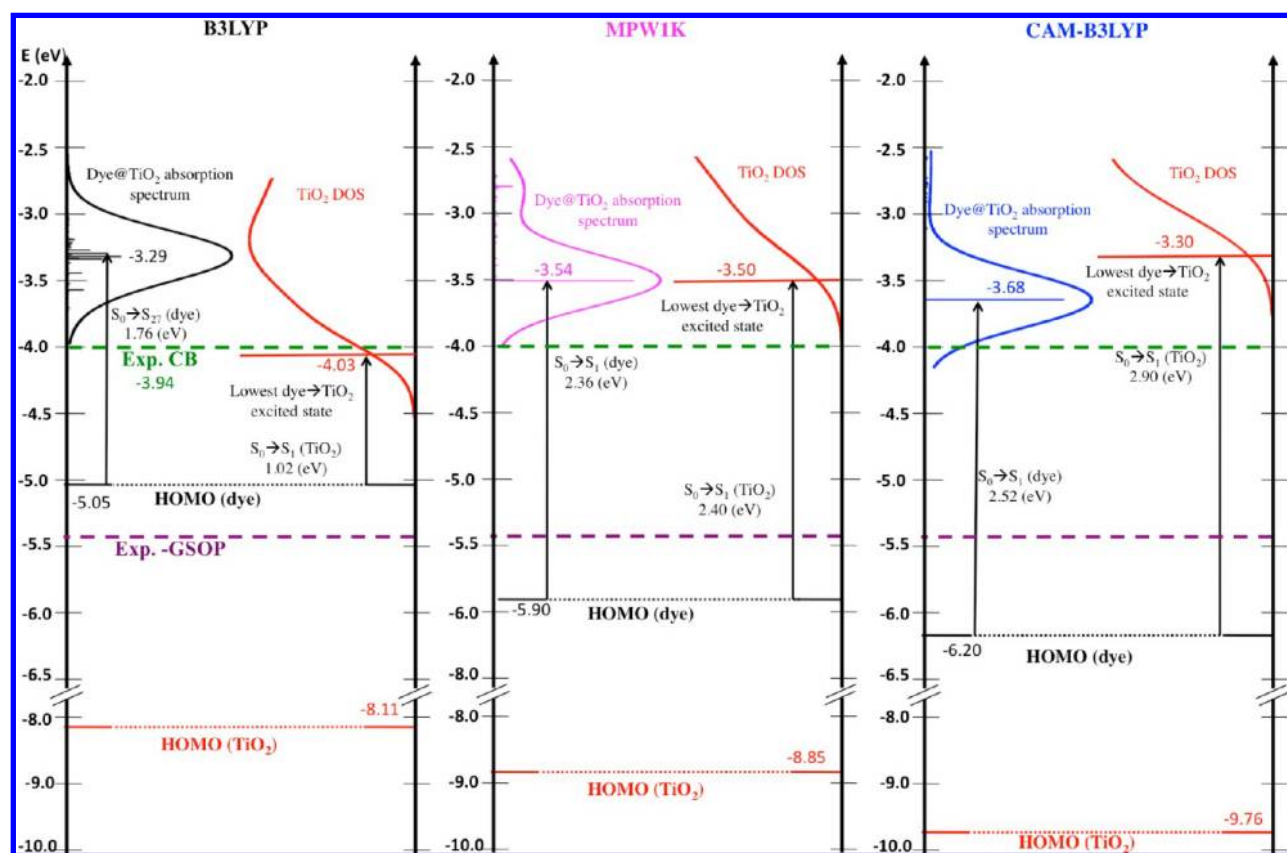We have presented an overview of computational modeling results aimed at understanding the fundamental parameters ruling the dye excited state electron injection into the semiconductor manifold of unoccupied states, which represent the primary charge generation event in dye-sensitized solar cells. The presented computational models, based on the use of large TiO$_2$ clusters, continuum solvation models, and an electronic structure description rooted into DFT/TDDFT

employing conventional hybrid and range-separated functional, have allowed us to reproduce to a good degree of accuracy the electronic and optical properties of both ruthenium dyes and fully organic dyes. For highly conjugated organic dyes, characterized by a high degree of charge transfer excited states, specifically tailored system-dependent exchange-correlation functionals are needed.

Moving to the description of dye/semiconductor interfaces, a successful strategy for ruthenium dyes@TiO$_2$ was presented, which accurately describes the electronic and optical properties *and* the alignment of ground and excited state levels at the same time. On the basis of this strategy, the nature, the coupling, and the energetics of the excited states underlying the ultrafast electron injection measured for this system have been thoroughly characterized. The key ingredients of this behavior are the very strong admixture of dye and semiconductor unoccupied states to form the dye-sensitized interface excited states and the optimal energetic positioning of the lowest interacting dye/semiconductor excited states compared to the TiO$_2$ manifold of unoccupied states.

For fully organic dyes, the problems associated to the charge-transfer nature of their excited states are transferred to their interaction with TiO$_2$. The specifically tailored methodology which allows us to solve these problems in solution works also on TiO$_2$, although different dyes, characterized by a variable conjugation across the donor–bridge–acceptor moieties, have a different response to the differently employed levels of theory. Our results show that at the single particle (i.e., LUMO) approximate level both the interfacial electronic coupling and

Figure 14. Alignment of the ground and excited state energy levels for the interacting JK2@TiO$_2$ system together with the calculated density of unoccupied TiO$_2$ states also aligned to the energy of the lowest TiO$_2$ state in the combined system. Green and purple dotted lines indicate the experimental TiO$_2$ CB edge and dye's GSOP, respectively. Notice that we have taken minus the value of GSOP to compare it to the dye's HOMO level.

the alignment of dye/semiconductor energy levels are not dramatically sensitive to the employed level of theory, delivering a reasonable, albeit approximate, picture of electron injection also for largely different organic dyes adsorbed onto TiO$_2$.

When shifting to the more appropriate excited state picture, however, we have shown that the explored DFT/TDDFT methods are not capable to deliver at the same time a balanced description of the dye@TiO$_2$ excited states and of the alignment of the dye excited states with the semiconductor manifold of unoccupied states for highly conjugated donor–acceptor push–pull dyes. This translates into an erroneous description of the relative energetics of dye/semiconductor excited states. As a matter of fact, with currently available x-c functionals, if one is able on the one hand to reproduce the optical absorption spectra of dye/TiO$_2$ assemblies by, e.g., range-separated methods, on the other hand the same methodology indicates a strongly energetically unfavorable electron injection pathway. By varying the exchange-correlation functional, a correct energy offset can be obtained, but a strongly underestimated absorption maximum energy is obtained. In perspective, we notice that intensive efforts are being devoted to solve the shortcomings of current TDDFT methodologies (see, e.g., ref 121 and references therein). In this framework, a promising approach appears to be the so-called optimized effective potential (OEP),[122−124] which however introduces a substantial increase of the computational overhead compared to standard x-c functionals. From a different perspective, accurate results for bulk materials as well as for charge transfer excitations in organic chromophores have been obtained using many-body Green's functions theory within the GW approximation and the Bethe–Salpeter equation (BSE). As the GW and GW-BSE approaches are significantly more computationally expensive than DFTs, their application to a problem of such a large size has been quite limited, and only recent advances in algorithms permitted a wider application.[2,125,126]

In conclusion, we believe that the correct and balanced description of push–pull organic dyes/semiconductor excited states, which is fundamental for modeling the primarily important light absorption and electron injection steps in dye-sensitized solar cells, still represents a challenge for theoretical and computational chemists and physicists which should be addressed by next-generation DFT or post-DFT methods.

■ AUTHOR INFORMATION

Corresponding Author

*E-mail: chiara@thch.unipg.it; filippo@thch.unipg.it. Phone: +39 075 585 5522. Fax: +39 075 585 5606.

Notes

The authors declare no competing financial interest.

Biographies

Mariachiara Pastore obtained her Ph.D. degree in 2009 in theoretical chemistry from University of Ferrara under the supervision of Prof. Renzo Cimiraglia, working on both methodological aspects, in the multireference perturbation methods field, and applications to the ab initio characterization of optical and structural properties of organic molecules. She took a postdoc position at Scuola Superiore ISUFI-University of Salento (Section Nanoscience - Grid Computing) concerning the "*modelling of organic molecules for solar cells applications*", working at Istituto CNR di Scienze e Tecnologie Molecolari (CNR-ISTM) in the research group of Dr. Filippo De Angelis. Currently, she is a senior postdoc at the Computational Laboratory for Hybrid/Organic Photovoltaics (CLHYO), at CNR-ISTM of Perugia. She is coauthor of 26 scientific papers published in International Journals. Her main research interests concern the computational modeling of the spectroscopic properties of dyes and dye/TiO_2 interfaces as well as methodological development of ab initio methods for excited state calculations.

Simona Fantacci is research scientist at the CNR Institute of Molecular Sciences and Technology, in Perugia, Italy. She is cofounder of the Computational Laboratory for Hybrid/Organic Photovoltaics (CLHYO) in Perugia. She received a Ph.D. in Theoretical Inorganic Chemistry from the University of Perugia in 1999 and was research associate at Princeton University (USA) in 2002−2003. Her research activity is focused on the theoretical investigation of the structural, electronic, and spectroscopic properties of complex systems containing transition metals by means of DFT and TDDFT methods with the ultimate goal to characterize their excited states. Her main research interests reside in the investigation of the electronic and linear and nonlinear optical properties of polypiridyl complexes of Ru(II) and Ir(III) employed in the fields of Dye-Sensitized Solar Cells, OLED devices, and NLO materials. Recently, she has been involved in the modeling of materials of interest in the Cultural Heritage field with the

aim to rationalize their photophysical properties and their degradation processes.

Filippo De Angelis is senior research scientist and deputy director at the CNR Institute of Molecular Sciences and Technology, in Perugia, Italy. He is the founder and coleader of the Computational Laboratory for Hybrid/Organic Photovoltaics in Perugia. He earned a B.S. in Chemistry 1996 and a Ph.D. in Theoretical Inorganic Chemistry in 1999, both from the University of Perugia, Italy. He is the 2007 recipient of the Raffaello Nasini Gold Medal of the Inorganic Chemistry Division of the Italian Chemical Society. He is an expert in the development and application of quantum chemical methods to the study of the structural, electronic, and optical properties of complex systems including transition metals. His main research interests are in the field of Dye-Sensitized Solar Cells, employing DFT, ab initio molecular dynamics, and TDDFT methods to predict and interpret the properties of organic and transition metal dyes. The interaction of dye sensitizers with nanostructured oxides and the evaluation of excited states for the interacting dye/semiconductor systems as well as modeling of the interface between dye-sensitized semiconductor and electrolytes and/or hole transporting materials are also actively investigated.

■ REFERENCES

(1) O'Regan, B.; Grätzel, M. *Nature* **1991**, *353*, 737−740.
(2) Pastore, M.; Mosconi, E.; De Angelis, F.; Grätzel, M. *J. Phys. Chem. C* **2010**, *114*, 7205−7212.
(3) De Angelis, F.; Fantacci, S.; Mosconi, E.; Nazeeruddin, M. K.; Grätzel, M. *J . Phys. Chem. C* **2011**, *115*, 8825−8831.
(4) Pastore, M.; Fantacci, S.; De Angelis, F. *J. Phys. Chem. C* **2010**, *114*, 22742−22750.
(5) De Angelis, F.; Fantacci, S.; Selloni, A. *Nanothec.* **2008**, *19*, 424002.
(6) O'Regan, B. C.; Walley, K.; Juozapavicius, M.; Anderson, A. Y.; Matar, F.; Ghaddar, T.; Zakeeruddin, S. M.; Klein, C.; Durrant, J. R. *J. Am. Chem. Soc.* **2009**, *131*, 3541−3548.
(7) O'Regan, B. C.; López-Duarte, I.; Martínez-Díaz, V.; Forneli, A.; Albero, J.; Morandeira, A.; Palomares, E.; Torres, T.; Durrant, J. R. *J. Am. Chem. Soc.* **2008**, *130*, 2906−2907.
(8) Wiberg, J.; Marinado, T.; Hagberg, D. P.; Sun, L.; Hagfeldt, A.; Albinsson, B. *J. Phys. Chem. C* **2009**, *113*, 3881−3886.
(9) Miyashita, M.; Sunahara, K.; Nishikawa, K.; Uemura, Y.; Koumura, N.; Hara, K.; Mori, A.; Abe, T.; Suzuki, E.; Mori, S. *J. Am. Chem. Soc.* **2008**, *130*, 17874−17881.
(10) Pastore, M.; De Angelis, F. *ACS Nano* **2010**, *4*, 556−562.

N

dx.doi.org/10.1021/jp3095227 | J. Phys. Chem. C XXXX, XXX, XXX−XXX

(11) Planells, M.; Pellejà, L.; Clifford, J. N.; Pastore, M.; De Angelis, F.; López, N.; Marder, S. R.; Palomares, E. *Energy Environ. Sci.* **2011**, *4*, 1820−1829.

(12) Hagberg, D. P.; Yum, J.-H.; Lee, H.; De Angelis, F.; Marinado, T.; Karlsson, K. M.; Humphry-Baker, R.; Sun, L.; Hagfeldt, A.; Grätzel, M.; et al. *J. Am. Chem. Soc.* **2008**, *130*, 6259−6266.

(13) Moser, J. E. Dynamics of Interfacial and Surface Electron Transfer Processes. In *Dye-Sensitized Solar Cells*; Kalyanasundaram, e. K., Ed.; EPFL Press: Lausanne, 2010; pp 403−456.

(14) Lanzafame, J. M.; Palese, S.; Wang, D.; Miller, R. J. D.; Muenter, A. A. *J . Phys. Chem* **1994**, *98*, 11020−11033.

(15) Hagfeldt, A.; Boschloo, G.; Sun, L.; Kloo, L.; Pettersson, H. *Chem. Rev.* **2010**, *110*, 6595−6663.

(16) Nazeeruddin, M. K.; De Angelis, F.; Fantacci, S.; Selloni, A.; Viscardi, G.; Liska, P.; Ito, S.; Takeru, B.; Grätzel, M. *J. Am. Chem. Soc.* **2005**, *127*, 16835−16847.

(17) Grätzel, M. *J. Photochem. Photobiol. A* **2004**, *164*, 3−14.

(18) Yella, A.; Lee, H.-W.; Tsao, H. N.; Yi, C.; Chandiran, A. K.; Nazeeruddin, M. K.; Diau, E. W.-G.; Yeh, C.-Y.; Grätzel, M. *Science* **2011**, *4*, 629−634.

(19) Hagberg, D. P.; Marinado, T.; Karlsson, K. M.; Nonomura, K.; Qin, P.; Boschloo, G.; Brinck, T.; Hagfeldt, A.; Sun, L. *J. Org. Chem.* **2007**, *72*, 9550−9556.

(20) Mishra, A.; Fischer, M.; Bäuerle, P. *Angew. Chem., Int. Ed.* **2009**, *48*, 2474−2499.

(21) Clifford, J. N.; Martínez-Ferrero, E.; Viterisi, A.; Palomares, E. *Chem. Soc. Rev.* **2011**, *40*, 1635−1646.

(22) Daeneke, T.; Kwon, T.-H.; Holmes, A. B.; Duffy, N. W.; Bach, U.; Spiccia, L. *Nat. Chem.* **2011**, *3*, 213−217.

(23) Feldt, S. M.; Gibson, E. A.; Gabrielsson, E.; Sun, L.; Boschloo, G.; Hagfeldt, A. *J. Am. Chem. Soc.* **2010**, *132*, 16714−16724.

(24) Feldt, S. M.; Cappel, U. B.; Johansson, E. M. J.; Boschloo, G.; Hagfeldt, A. *J. Phys. Chem. C* **2010**, *114*, 10551−10558.

(25) Bai, Y.; Zhang, J.; Zhou, D.; Wang, Y.; Zhang, M.; Wang, P. *J. Am. Chem. Soc.* **2011**, *133*, 11442−11445.

(26) Cameron, P. J.; Peter, L. M.; Zakeeruddin, S. M.; Grätzel, M. *Coord. Chem. Rev.* **2004**, *248*, 1447−1453.

(27) De Angelis, F.; Fantacci, S.; Sgamellotti, A. *Theor. Chem. Acc.* **2007**, *117*, 1093−1104.

(28) Lee, D. H.; Lee, M. J.; Song, H. M.; Song, B. J.; Seo, K. D.; Pastore, M.; Anselmi, C.; Fantacci, S.; De Angelis, F.; Nazeeruddin, M. K.; et al. *Dyes Pigm.* **2011**, *91*, 192−198.

(29) Stier, W.; Prezhdo, O. V. *J. Phys. Chem. B* **2002**, *106*, 8047−8054.

(30) Rego, L. G. C.; Batista, V. S. *J. Am. Chem. Soc.* **2003**, *125*, 7989−7997.

(31) Kondov, I.; Čížek, M.; Benesch, C.; Wang, H.; Thoss, M. *J . Phys. Chem. C* **2007**, *111*, 11970−11981.

(32) Meng, S.; Ren, J.; Kaxiras, E. *Nano Lett.* **2008**, *8*, 3266−3272.

(33) Rego, L. G. C.; Batista, V. S. *J. Am. Chem. Soc.* **2003**, *125*, 7989−7997.

(34) Abuabara, S. G.; Rego, L. G. C.; Batista, V. S. *J. Am. Chem. Soc.* **2005**, *127*, 18234−18242.

(35) Hoff, D. A.; da Silva, R.; Rego, L. G. C. *J. Phys. Chem. C* **2012**, *116*, 21169−21178.

(36) Duncan, W. R.; Stier, W. M.; Prezhdo, O. V. *J. Am. Chem. Soc.* **2005**, *127*, 7941−7795.

(37) Li, J.; Wang, H.; Persson, P.; Thoss, M. *J. Chem. Phys.* **2012**, *137*, 22A529.

(38) Duncan, W. R.; Stier, W. M.; Prezhdo, O. V. *J. Am. Chem. Soc.* **2005**, *127*, 7941−7951.

(39) Marques, M. A. L.; López, X.; Varsano, D.; Castro, A.; Rubio, A. *Phys. Rev. Lett.* **2003**, *90*, 258101−258104.

(40) Meng, S.; Kaxiras, E. *Nano Lett.* **2010**, *10*, 1238−1247.

(41) Fantacci, S.; De Angelis, F.; Selloni, A. *J. Am. Chem. Soc.* **2003**, *125*, 4381−4387.

(42) De Angelis, F.; Fantacci, S.; Selloni, A. *Chem. Phys. Lett.* **2005**, *415*, 115−120.

(43) De Angelis, F.; Fantacci, S.; Selloni, A. *Chem. Phys. Lett.* **2004**, *389*, 204.

(44) De Angelis, F.; Fantacci, S.; Selloni, A.; Nazeeruddin, M. K.; Grätzel, M. *J. Am. Chem. Soc.* **2007**, *129*, 14156−14157.

(45) De Angelis, F.; Fantacci, S.; Selloni, A.; Grätzel, M.; Nazeeruddin, M. K. *Nano Lett.* **2007**, *7*, 3189−3195.

(46) De Angelis, F.; Fantacci, S.; Selloni, A.; Nazeeruddin, M. K.; Grätzel, M. *J. Phys. Chem. C* **2010**, *114*, 6054−6061.

(47) De Angelis, F.; Fantacci, S.; Gebauer, R. *J. Phys. Chem. Lett.* **2011**, *2*, 813−817.

(48) Abbotto, A.; Barolo, C.; Bellotto, L.; De Angelis, F.; Grätzel, M.; Manfredi, N.; Marinzi, C.; Fantacci, S.; Yum, J.; Nazeeruddin, M. K. *Chem. Commun.* **2008**, 5318−5320.

(49) Becke, A. D. *J. Chem. Phys.* **1993**, *98*, 1372−1377.

(50) Kalyanasundaram, K.; Grätzel, M. *Coord. Chem. Rev.* **1998**, *177*, 347.

(51) Haque, S. A.; Palomares, E.; Cho, B. M.; Green, A. N. M.; Hirata, N.; Klug, D. R.; Durrant, J. R. *J. Am. Chem. Soc.* **2005**, *127*, 3456−3462.

(52) Rohrdanz, M. A.; Herbert, J. M. *J. Chem. Phys.* **2008**, *129*, 034107−034109.

(53) Lange, A. W.; Rohrdanz, M. A.; Herbert, J. M. *J. Phys. Chem. B* **2008**, *112*, 6304−6308.

(54) Pastore, M.; Mosconi, E.; Fantacci, S.; De Angelis, F. *Curr. Org. Synth.* **2012**, *9*, 215−232.

(55) Cossi, M.; Barone, V. *J. Chem. Phys.* **2001**, *115*, 4708−4717.

(56) Mosconi, E.; Selloni, A.; De Angelis, F. *J. Phys. Chem. C* **2012**, *116*, 5932−5940.

(57) Gebauer, R.; De Angelis, F. *New. J. Phys.* **2011**, *13*, 085013.

(58) Manzhos, S.; Segawa, H.; Yamashita, K. *Phy. Chem. Chem. Phys.* **2012**, *14*, 1749−1755.

(59) Klamt, A.; Schüürmann, G. *J. Chem. Soc., Perkin Trans. 2* **1993**, 799−805.

(60) Schiffmann, F.; VandeVondele, J.; Hutter, J. r.; Wirz, R.; Urakawa, A.; Baiker, A. *J. Phys. Chem. C* **2010**, *114*, 8398−8404.

(61) Cardona, C. M.; Li, W.; Kaifer, A. E.; Stockdale, D.; Klug, R.; Bazan, G. C. *Adv. Mater.* **2011**, *23*, 2367−2371.

(62) Frisch, M. J.; Trucks, G. W.; Schlegel, H. B.; Scuseria, G. E.; Robb, M. A.; Cheeseman, J. R.; Montgomery, J. A.; Vreven, J., T. ; Kudin, K. N.; Burant, J. C.,et al. *Gaussian 03*, revision B05; Gaussian Inc.: Pittsburgh PA, 2003.

(63) Lynch, B. J.; Fast, P. L.; Harris, M.; Truhlar, D. G. *J. Phys. Chem. A* **2000**, *104*, 4811.

(64) Frisch, M. J.; Trucks, G. W.; Schlegel, H. B.; Scuseria, G. E.; Robb, M. A.; Cheeseman, J. R.; Scalmani, G.; Barone, V.; Mennucci, B.; Petersson, G. A., et al. *Gaussian 09*, revision A.1; Gaussian, Inc.: Wallingford CT, 2009.

(65) Alhrichs, R.; et al. *TURBOMOLE*, v. 5.10; University of Karlsruhe: Germany.

(66) Furche, F.; Ahlrichs, R. *J. Chem. Phys.* **2002**, *117*, 7433.

(67) Schäfer, A.; Horn, H.; Ahlrichs, R. *J. Chem. Phys.* **1992**, *97*, 2571.

(68) Becke, A. D. *J. Chem. Phys.* **1993**, *98*, 5648−5652.

(69) Becke, A. D. *Phys. Rev. A* **1988**, *38*, 3098−3100.

(70) Lee, C.; Yang, W.; Parr, R. G. *Phys. Rev. B* **1988**, *37*, 785−789.

(71) Wolfbauer, G.; Bond, A. M.; Deacon, G. B.; MacFarlane, D. R.; Spiccia, L. *J. Am. Chem. Soc.* **2000**, *122*, 130−142.

(72) Jacquemin, D.; Perpète, E. A.; Ciofini, I.; Adamo, C. *Acc. Chem. Res.* **2009**, *42*, 326−334.

(73) Jacquemin, D.; Perpete, E. A.; Scuseria, G. E.; Ciofini, I.; Adamo, C. *J. Chem. Theory Comput.* **2008**, *4*, 123−135.

(74) Dreuw, A.; Weisman, J. L.; Head-Gordon, M. *J. Chem. Phys.* **2003**, *119*, 2943−2946.

(75) Tozer, D. J. *J. Chem. Phys.* **2003**, *119*, 12697−12699.

(76) Dev, P.; Agrawal, S.; English, N. J. *J. Chem. Phys.* **2012**, *136*, 224301.

(77) Tawada, Y.; Tsuneda, T.; Yanagisawa, S.; Yanai, T.; Hirao, K. *J. Chem. Phys.* **2004**, *120*, 8425−8433.

(78) Kamiya, M.; Sekino, H.; Tsuneda, T.; Hirao, K. *J. Chem. Phys.* **2005**, *122*, 234111.

O

dx.doi.org/10.1021/jp3095227 | *J. Phys. Chem. C* XXXX, XXX, XXX−XXX

(79) Iikura, H.; Tsuneda, T.; Yanai, T.; Hirao, K. *J. Chem. Phys.* **2001**, *115*, 3540−3544.

(80) Chai, J.-D.; Head-Gordon, M. *J. Chem. Phys.* **2008**, *128*, 084106.

(81) Yanai, T.; Tew, D. P.; Handy, N. C. *Chem. Phys. Lett.* **2004**, *393*, 51−57.

(82) Kim, S.; Lee, J. K.; Kang, S. O.; Ko, J.; Yum, J. H.; Fantacci, S.; De Angelis, F.; Di Censo, D.; Nazeeruddin, M. K.; Grätzel, M. *J. Am. Chem. Soc.* **2006**, *128*, 16701−16707.

(83) Schmidt-Mende, L.; Bach, U.; Humphry-Baker, R.; Horiuchi, T.; Miura, H.; Ito, S.; Uchida, S.; Grätzel, M. *Adv. Mater.* **2005**, *17*, 813−815.

(84) Horiuchi, T.; Miura, H.; Uchida, S. *Chem. Commun.* **2003**, 3036−3037.

(85) Magyar, R. J.; Tretiak, S. *J. Chem. Theory Comput.* **2007**, *3*, 976−987.

(86) Preat, J.; Michaux, C.; Jacquemin, D.; Perpete, E. A. *J. Phys. Chem. C* **2009**, *113*, 16821−16833.

(87) Wiggins, P.; Williams, J.; Tozer, D. *J. Chem. Phys.* **2009**, *131*, 091101.

(88) Plotner, J.; Dreuw, A. *Chem. Phys.* **2008**, *347*, 472−482.

(89) Plotner, J.; Tozer, D. J.; Dreuw, A. *J. Chem. Theory Comput.* **2010**, 1−10.

(90) Martsinovich, N.; Troisi, A. *Energy Environ. Sci.* **2011**, *4*, 4473−4495.

(91) Pastore, M.; De Angelis, F. *Phys. Chem. Chem. Phys.* **2012**, *14*, 920−928.

(92) Nara, M.; Torii, H.; Tasumi, M. *J. Phys. Chem.* **1996**, *100*, 19812−19817.

(93) Deacon, G. B.; Phillips, R. J. *Coord. Chem. Rev.* **1980**, *33*, 227−250.

(94) Shklover, V.; Ovchinnikov, Y. E.; Braginsky, L. S.; Zakeeruddin, S. M.; Grätzel, M. *Chem. Mater.* **1998**, *10*, 2533−2541.

(95) Srinivas, K.; Yesudas, K.; Bhanuprakash, K.; Rao, V. J.; Giribabu, L. *J. Phys. Chem. C* **2009**, *113*, 20117−20126.

(96) Pérez León, C.; Kador, L.; Peng, B.; Thelakkat, M. *J. Phys. Chem. B* **2006**, *110*, 8723−8730.

(97) Chen, P.; Yum, J. H.; Angelis, F. D.; Mosconi, E.; Fantacci, S.; Moon, S.-J.; Baker, R. H.; Ko, J.; Nazeeruddin, M. K.; Grätzel, M. *Nano Lett.* **2009**, *9*, 2487−2492.

(98) De Angelis, F.; Fantacci, S.; Selloni, A.; Nazeeruddin, M. K.; Grätzel, M. *J. Phys. Chem. C* **2010**, *114*, 6054−6061.

(99) Rocca, D.; Gebauer, R.; De Angelis, F.; Nazeeruddin, M. K.; Baroni, S. *Chem. Phys. Lett.* **2009**, *475*, 49−53.

(100) Martsinovich, N.; Jones, D. R.; Troisi, A. *J. Phys. Chem. C* **2010**, *114*, 22659−22670.

(101) Martsinovich, N.; Troisi, A. *J. Phys. Chem. C* **2011**, *115*, 11781−11792.

(102) De Angelis, F. *Chem. Phys. Lett.* **2010**, *493*, 323−327.

(103) Persson, P.; Bergstrom, R.; Lunell, S. *J. Phys. Chem. B* **2000**, *104*, 10348−10351.

(104) Vittadini, A.; Selloni, A.; Rotzinger, F. P.; Grätzel, M. *J. Phys. Chem. B* **2000**, *104*, 1300−1306.

(105) Tian, H.; Yang, X.; Chen, R.; Zhang, R.; Hagfeldt, A.; Sun, L. *J. Phys. Chem. C* **2008**, *112*, 11023−11033.

(106) Pastore, M.; De Angelis, F. *J. Phys. Chem. Lett.* **2011**, *2*, 1261−1267.

(107) Nunzi, F.; De Angelis, F. *J. Phys. Chem. C* **2011**, *115*, 2179−2186.

(108) Car, R.; Parrinello, M. *Phys. Rev. Lett.* **1985**, *55*, 2471−2474.

(109) Giannozzi, P.; Baroni, S.; Bonini, N.; Calandra, M.; Car, R.; Cavazzoni, C.; Ceresoli, D.; Chiarotti, G. L.; Cococcioni, M.; Dabo, I.; et al. *J. Phys.: Condens. Matter* **2009**, *21*, 395502.

(110) Perdew, J. P.; Burke, K.; Ernzerhof, M. *Phys. Rev. Lett.* **1996**, *77*, 3865−3868.

(111) De Angelis, F.; Tilocca, A.; Selloni, A. *J. Am. Chem. Soc.* **2004**, *126*, 15024−15025.

(112) Griffith, M. J.; James, M.; Triani, G.; Wagner, P.; Wallace, G. G.; Officer, D. L. *Langmuir* **2011**, *27*, 12944−12950.

(113) te Velde, G.; Bickelhaupt, F. M.; Baerends, E. J.; Fonseca Guerra, C.; van Gisbergen, S. J. A.; Snijders, J. G.; Ziegler, T. *J. Comput. Chem.* **2001**, *22*, 931−967.

(114) Perdew, J. P. *Phys. Rev. B* **1986**, *33*, 8822−8824.

(115) Lundqvist, M. J.; Nilsing, M.; Persson, P.; Lunel, S. *Int. J. Quantum Chem.* **2006**, *106*, 3214−3234.

(116) Benkö, G.; Kallioinen, J.; Korppi-Tommola, J. E. I.; Yartsev, A. P.; Sundström, V. *J. Am. Chem. Soc.* **2002**, *124*, 489−493.

(117) Bräm, O.; Cannizzo, A.; Chergui, M. *Phys. Chem. Chem. Phys.* **2012**, *14*, 7934−7937.

(118) Persson, P.; Lundqvist, M. J. *J. Phys. Chem. B* **2005**, *109*, 11918.

(119) Rothenberger, G.; Fitzmaurice, D.; Grätzel, M. *J. Phys. Chem.* **1992**, *96*, 5983−5986.

(120) Redmond, G.; Fitzmaurice, D. *J. Phys. Chem.* **1993**, *97*, 1426−1430.

(121) Casida, M. E.; Huix-Rotllant, M. *Annu. Rev. Phys. Chem.* **2012**, *63*, 287−323.

(122) Ullrich, C. A.; Gossmann, U. J.; Gross, E. K. U. *Phys. Rev. Lett.* **1995**, *74*, 872−875.

(123) Görling, A. *Int. J. Quantum Chem.* **1998**, *69*, 265−277.

(124) Hirata, S.; Ivanov, S.; Grabowski, I.; Bartlett, R. J. *J. Chem. Phys.* **2002**, *116*, 6468−6482.

(125) Umari, P.; Stenuit, G.; Baroni, S. *Phys. Rev. B* **2010**, *81*, 115104−115109.

(126) Baumeier, B.; Andrienko, D.; Rohlfing, M. *J. Chem. Theory Comput.* **2012**, *8*, 2790−2795.